

## Article

# Remote Sensing-Based Dynamic Monitoring of Immovable Cultural Relics, from Environmental Factors to the Protected Cultural Site: A Case Study of the Shunji Bridge

Yanzhen Liu <sup>1</sup>, Yunwei Tang <sup>2,\*</sup>, Linhai Jing <sup>2</sup>, Fulong Chen <sup>2</sup> and Ping Wang <sup>1</sup>

<sup>1</sup> College of Geodesy and Geomatics, Shandong University of Science and Technology, Qingdao 266590, China; 201883020041@sdust.edu.cn (Y.L.); skd990058@sdust.edu.cn (P.W.)

<sup>2</sup> Key Laboratory of Digital Earth Science, Aerospace Information Research Institute, Chinese Academy of Sciences, Beijing 100094, China; jinglh@aircas.ac.cn (L.J.); chenfl@aircas.ac.cn (F.C.)

\* Correspondence: tangyw@aircas.ac.cn

**Abstract:** This paper explores the ability of remote sensing techniques to monitor immovable cultural relics on multiple scales. The Shunji Bridge, a destroyed cultural relic, located in the Jinjiang River Basin, Fujian Province, China, was studied in terms of the environmental factors at the macroscale and the protected cultural site at the microscale. At the macroscale, moderate spatial resolution images of the Jinjiang River Basin were processed in the Google Earth Engine (GEE) platform to extract environmental factors, such as land cover and vegetation cover. At the microscale, Google Earth time series images were used to extract attribute information to reflect the spatial and temporal changes in the Shunji Bridge before, during and after its destruction. Quantitative assessment of the Shunji Bridge was performed to assess the degree of the impacts that different factors had on the immovable cultural relic. Spatial analysis methods were applied to trace back to the source of the bridge destruction and to track the situation after the bridge was destroyed. The causes of the destruction of the bridge are revealed at both the macro- and microscales. This study provides technical support for the natural disaster risk assessment of immovable cultural relics. The findings of this research can provide suggestions for the protection of immovable cultural relics.

**Keywords:** cultural heritage; remote sensing; dynamic monitoring; environmental factors



**Citation:** Liu, Y.; Tang, Y.; Jing, L.; Chen, F.; Wang, P. Remote Sensing-Based Dynamic Monitoring of Immovable Cultural Relics, from Environmental Factors to the Protected Cultural Site: A Case Study of the Shunji Bridge. *Sustainability* **2021**, *13*, 6042. <https://doi.org/10.3390/su13116042>

Academic Editors: Ioannis Liritzis and John Carman

Received: 5 April 2021  
Accepted: 25 May 2021  
Published: 27 May 2021

**Publisher's Note:** MDPI stays neutral with regard to jurisdictional claims in published maps and institutional affiliations.



**Copyright:** © 2021 by the authors. Licensee MDPI, Basel, Switzerland. This article is an open access article distributed under the terms and conditions of the Creative Commons Attribution (CC BY) license (<https://creativecommons.org/licenses/by/4.0/>).

## 1. Introduction

Cultural heritage is the accumulation and essence of the development of human civilization; it is a rare and irreplaceable wealth endowed by history [1–3]. Recording and protecting cultural heritage is a common responsibility and obligation of all people. With the development of society and the deterioration of natural environments, natural and artificial risk factors that pose serious threats to cultural heritage are increasing [4–8]. When natural disasters such as earthquakes, floods and landslides occur, they can catastrophically impact cultural heritage [9]. For this reason, research on cultural heritage protection has received considerable attention in recent years [10–13].

Spatial information technology developed in the mid-to-late 20th century brought an opportunity to improve cultural heritage monitoring. Remote sensing techniques have shown advantages over traditional manual work in monitoring cultural heritage. For example, detection using remote sensing techniques are non-destructive, and remote sensing data are easier to obtain and much lower in cost than data collected by manual work. Remote sensing can realize rapid multiscale exploration and mapping, rapid multisource data analysis, and the dynamic monitoring of cultural relics and their surrounding environments [14]. Remote sensing has, therefore, been favoured by researchers in recent years and has become a new tool for cultural heritage protection [15] and management [16–20].

Immovable cultural relics refer to specific historical and cultural sites, architecture and art [21], including ancient buildings, ancient sites, and historical and cultural artefacts.

The observation of immovable cultural relics, as an important part of cultural heritage, using remote sensing techniques has become possible with the enhancement of the spatial and temporal resolution of satellite images [22]. Commonly, dynamic monitoring of environmental factors at the macroscale is performed and the change information of protected cultural sites at the microscale are analysed to provide useful information to guide the protection of immovable cultural relics.

Researchers have monitored different environmental factors, such as vegetation indices, topography, climate variables, and land cover maps, to analyse the surrounding environments of immovable cultural relics [23]. For example, Banerjee and Srivastava evaluated land cover and land use changes around cultural sites in central India using Landsat series images [24]. Bai et al. analysed spatial and temporal changes in land cover classes in one of the World Heritage sites on Mount Wutai and its environment, based on multi-source remote sensing images, including moderate-resolution imaging spectroradiometer (MODIS) normalized difference vegetation index (NDVI) products, Landsat series images and advanced spaceborne thermal emission and reflection radiometer (ASTER) digital elevation model (DEM) data [25]. Assassi and Mebarki analysed the spatial configuration of the ancient town of Timgad for urban and architectural planning [26]. According to the derived environmental factors, some researchers focused on studying the impact of natural disasters and human activity on immovable cultural relics. Diwan extracted six environmental factors to produce predictive maps for Iron Age sites in Bekaa, Lebanon [27]. Based on the Corine Land Cover dataset and GlobCover data of cultural sites and the nearby areas in Cyprus, Hadjimitsis et al. applied spatial analysis to monitor the impact of disasters on cultural sites and their surrounding environment and conducted risk assessments [28]. In 2015, Agapiou et al. used Landsat series images to classify the environment surrounding the Paphos area in Cyprus, revealing the impact of urban expansion on immovable cultural relics [29]. Environmental monitoring usually requires a large area to be observed so that low or moderate spatial resolution images are used. To process these images, professional software is necessary to implement data pre-processing [30,31] (e.g., radiation calibration and atmospheric correction) and information extraction (e.g., principal component analysis, filtering, and classification). Traditional software, such as ENVI and ArcGIS, takes a long time and is relatively inefficient in the processing of massive data, thus limiting the application of remote sensing. Google Earth Engine (GEE) is a non-profit platform that has powerful capabilities for image processing and massive computing. For example, Chen et al. used GEE to calculate an ecological index that can reflect the quality of the ecological environment based on thousands of Landsat TM images, and then assessed the eco-environment quality in the Three Rivers Source Region [32]. Generally, however, GEE has not been fully utilized for cultural preservation. Therefore, it is necessary to explore the potential of GEE to efficiently handle a large amount of remote sensing data in the field of cultural preservation.

In terms of protected cultural site monitoring, researchers used various remote sensing images to extract the boundaries of cultural heritage sites. In earlier times, the most commonly used images were Landsat series images. Aminzadeh and Samani used Landsat 7 Enhanced Thematic Mapper Plus (ETM+) images to identify the boundaries of historical sites in Persepolis [33]. Themistocleous et al. conducted a multi-temporal analysis of historical sites in Cyprus and showed the feasibility of using remote sensing to monitor historical sites [34]. Then, high spatial resolution images have shown advantages in fine monitoring of cultural heritage sites. In 2014, Figorito and Tarantino detected and extracted historical sites from time series aerial images and achieved good results [35]. In the same year, Luo et al. extracted the relics of the Dunhuang imperial road in the Hexi Corridor based on remote sensing image interpretation, geographic information system (GIS) analysis and field surveys [36]. In recent years, unmanned aerial vehicles (UAVs) and light detection and ranging (LiDAR) have become increasingly common methods for researchers to investigate historical sites [37–39]. LiDAR data include height and structure information of ground objects and can be used to reconstruct cultural sites [40]. Trier

used a faster region-convolutional neural network (R-CNN) and airborne LiDAR data to draw a map of Norwegian cultural heritage [41]. Cultural heritages can be recorded, visualized and reconstructed based on 3D modelling by using a digital camera and LiDAR scanner [42]. In 2017, Hatzopoulos et al. performed 3D digital modelling of the Tholos monument in Greece [43]. In the same year, the historical masonry arch, Dokuzunhan Bridge, was measured for 3D modelling by Altuntas et al. [44]. However, LiDAR is costly, and the available data are limited. Alternatively, UAVs can capture high spatial resolution images at a low cost [45]. In 2019, Su et al. used UAV images to monitor the Huangwei site in Jinmen, Taiwan, China. Through the analysis of weather, topography and other factors using GIS, the environmental risks were evaluated, and an environmental risk map was created to reveal the potential environmental risks of the study site [46]. In general, most existing studies on monitoring protected cultural sites can only reach the scale at large buildings, such as ancient buildings and cave temples [33,34,36,46]. It is rare to monitor cultural sites at a finer scale, such as bridges. In addition, superior to UAV images, Google Earth images not only have a high spatial resolution but also the historical images can be obtained without any cost. Currently, however, Google Earth historical images have not been fully used in monitoring cultural heritage sites. Therefore, it is possible to explore the potential of Google Earth images to monitor the cultural relics of small areas.

In the current research on cultural heritage protection, most research has focused on a single scale. For example, Zhen et al. evaluated the impact of climate change and human disturbance on giant panda habitat in the core area of a heritage site in Ya'an, China [47]. Roy et al. assessed the geographical environment of Majuli Island in Assam and sought effective measures to protect the island from further erosion by the Brahmaputra and its tributaries [48]. These studies either analysed the environment scale or the protected site scale, while the effects at both the macro- and microscales are important. In addition, most of the research focuses on risk assessment and risk map production [49–51]. There is a lack of research on tracking the impacts of disasters on cultural relics.

In summary, in terms of the dynamic monitoring of immovable cultural relics using remote sensing, the current research mainly faces the following shortcomings. First, sub-meter spatial resolution remote sensing images are not fully used, especially Google Earth historical images. The utilization of sub-meter-resolution images has the potential to observe small cultural sites. Second, when monitoring environmental factors surrounding the cultural site, the images are often processed by some popular remote sensing software, which is time-consuming and laborious. Most non-remote-sensing researchers are unfamiliar with some advanced data processing tools, such as the GEE platform. Third, most of the current research focuses on spatial archaeology and environmental risk assessment. There is a lack of research on the whole process of disaster monitoring, such as tracing the source of the disaster or tracking the situation after the disaster.

Therefore, this study carried out environmental factor monitoring and immovable cultural relic detection at both the macro- and microscales. In terms of environmental factor monitoring, remote sensing images with moderate spatial resolution were used to extract various environmental factors by the GEE platform. In terms of cultural relic monitoring, Google Earth time series images with a sub-meter spatial resolution were used to extract the attribute information to reflect the changes before and after destruction. A ruined immovable cultural relic, the Shunji Bridge, was studied in this paper. Quantitative assessment of the Shunji Bridge ranging from environmental factors at the macroscale to the protected cultural site at the microscale was performed. The whole process of the destruction of the bridge was traced, and the causes of its destruction were analysed. The findings can provide technical support for the risk assessment of and emergency response to natural disasters.

## 2. Materials and Methods

### 2.1. Study Area

The Shunji Bridge, built in 1211 during the Southern Song Dynasty, is a protected cultural site and a microcosm of the construction history in Quanzhou. The Shunji Bridge is located in the lower reaches of Jinjiang, Licheng District, Quanzhou, Fujian Province. This bridge is a typical ancient Chinese bridge. It provides important archaeological data for the study of the development of ancient bridges, such as the structures of bridges and the history of water transportation. The bridge has been repaired many times since the 14th century. In July 2006, the Shunji Bridge was destroyed by Typhoon Bilis. In September 2010, because of Typhoon Fanapi, the bridge collapsed again and lost its ability to handle traffic. The government of Quanzhou decided to restore the Shunji Bridge as a pedestrian bridge in November 2011. However, due to the shortage of funds, the restoration was suspended. This bridge has been preserved as a ruin up to the present. In January 2020, the Shunji Bridge was listed in the ninth batch of provincial protected cultural sites by the People's Government of Fujian Province. In this study, spatial and temporal changes in the Shunji Bridge were studied at the microscale.

The Jinjiang River Basin is approximately 5630 km<sup>2</sup>. Rugged hills and coastal plains cover much of the basin. This area mainly features a subtropical maritime monsoon climate. The seasons are distinct, with dry winters and rainy summers. The Jinjiang River originates from Daiyun Mountain in the central Fujian Province. Its length is approximately 182 km. The river divides into many branches; thus, the drainage network is dense. Two main branches, Dongxi and Xixi, flow into the upper reaches of the river. The lower reaches of the Jinjiang River, located near the East China Sea, are low-lying and habitable. Due to rapid development, this area suffers from serious water loss and soil erosion. As a consequence, the rainstorms in the rainy season (from June to September) usually cause flooding in the lower reaches of the Jinjiang River. Environmental factors were extracted and analysed at the macroscale in the Jinjiang River Basin.

### 2.2. Experimental Data

#### 2.2.1. Data for Monitoring Environmental Factors

Landsat 7 ETM+ images, Sentinel-2 images, and Advanced Land Observing Satellite (ALOS) DEM data were used to monitor four environmental factors: land cover classes, vegetation cover, topography and soil erosion information.

Historical land cover classes and vegetation cover data were extracted from Landsat 7 ETM+ and Sentinel-2 images from three years: 2000, 2010, and 2019. Due to the unavailability of Sentinel-2 images before the satellite launch in 2015, Landsat 7 ETM+ images were selected for the first two periods. The Landsat 7 ETM+ sensor has 8 multispectral bands, covering visible to infrared wavelengths. The spatial resolution of the multispectral bands is 30 m, except for the thermal infrared band, which has a spatial resolution of 60 m. The Sentinel-2 images include 13 multispectral bands with spatial resolutions of 10 m, 20 m and 60 m. The multispectral bands at 20 m and 60 m were all resampled to 10 m. Images of the Jinjiang River Basin area with low cloud cover were selected. Four images from both Landsat 7 ETM+ and Sentinel-2 are needed to cover this area. Images from different years were selected in the same season to guarantee similar vegetation growth.

GEE is a cloud computing platform for processing satellite images. It provides access to a large database of satellite images and considerable computational power to process images. Moderate spatial resolution images, such as Landsat and Sentinel-2 images are easily accessed and processed using GEE. The pre-processing steps of the Landsat 7 ETM+ and Sentinel-2 images, including radiation correction, image fusion, multispectral band resampling, image mosaicking and image cutting, were all implemented in GEE.

ALOS DEM images were used to extract topographic information. The spatial resolution of the ALOS DEM is 12.5 m. Six ALOS DEM images are required to cover this area. The pre-processing of the DEM images, including image mosaicking and image cutting, was performed on an offline platform.

The images used for monitoring environmental factors in the Jinjiang River Basin are shown in Figure 1. Information on the selected images is listed in Table 1.

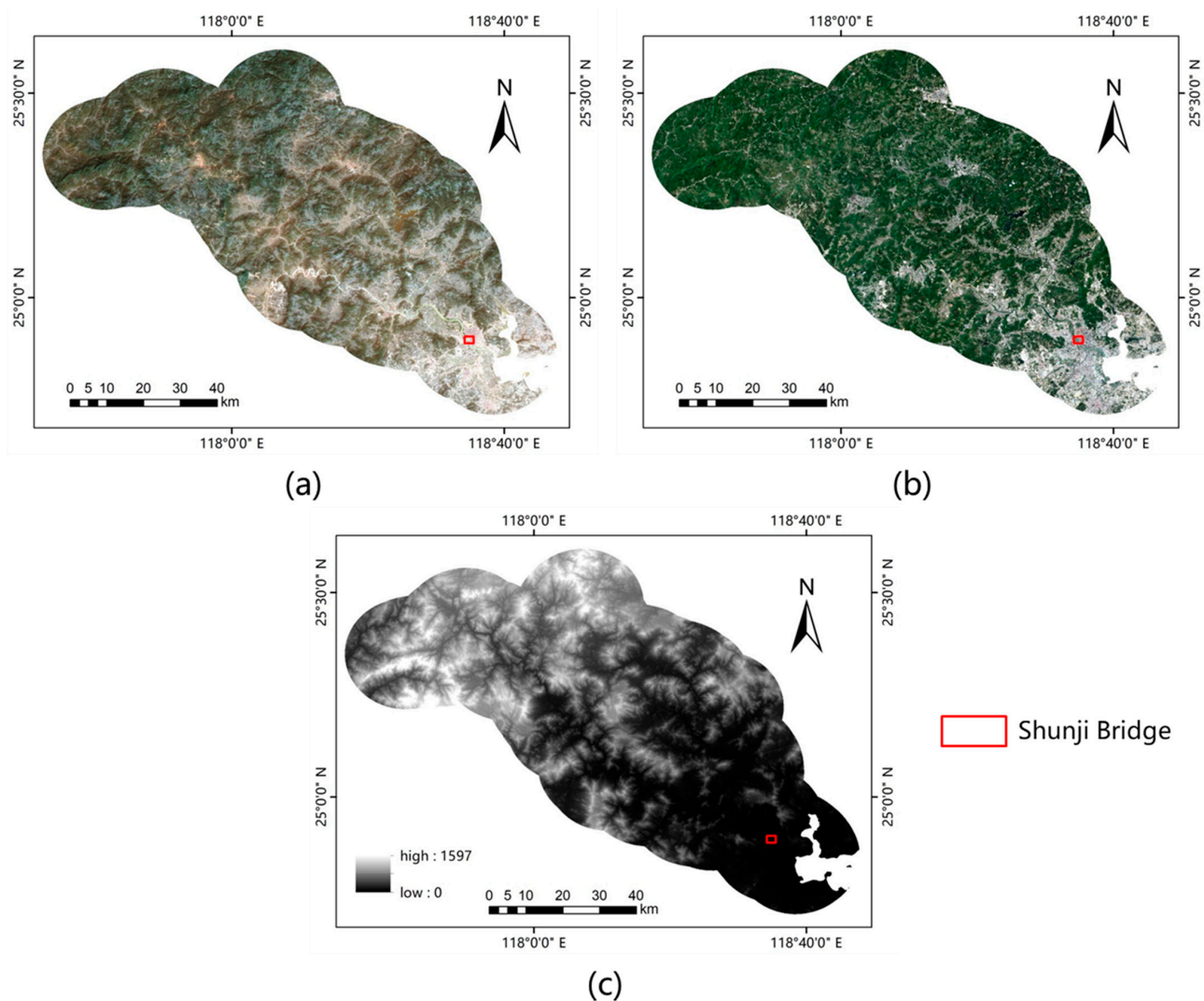


**Figure 1.** Images used for monitoring environmental factors in the Jinjiang River Basin. (a) Landsat 7 ETM+ image, (b) Sentinel-2 image, (c) ALOS DEM data.

**Table 1.** Information on the images used for monitoring environmental factors.

Data	Spatial Resolution	Acquisition Time	Purpose
Landsat-7 ETM+	30 m	September to November 2000, 2010	Land cover classification and vegetation cover information extraction.
Sentinel-2	10 m	September to November 2019	
ALOS DEM	12.5 m	2007	Topographic information extraction.

### 2.2.2. Data for Monitoring the Protected Cultural Site

In 1998, to alleviate the traffic pressure on the Shunji Bridge, the government built a new bridge called the Shunji New Bridge, which is located 80 m upriver from the Shunji Bridge. Considering the rather close proximity, the two bridges were monitored and analysed together. Google Earth time series images were used to monitor the protected

cultural site. Since there is a lack of Google Earth images before the Shunji New Bridge was built, a Landsat 5 Thematic Mapper (TM) image from 1996 was selected. Information on the selected images is listed in Table 2.

**Table 2.** Information on the images used for monitoring the protected cultural site.

Data	Spatial Resolution	Acquisition Time	Purpose
Landsat-5 TM	30 m	1996	Attribute information measurement.
Google Earth	0.27 m	2002, 2006, 2009, 2011, 2012, 2013, 2014, 2015, 2016, 2017	

Similar to the Landsat 7 ETM+, the Landsat 5 TM sensor has 7 multispectral bands. The spatial resolution of the multispectral bands is 30 m, and the thermal infrared band has a spatial resolution of 60 m. Since the Landsat 5 TM image does not include the panchromatic band, multispectral images with a spatial resolution of 30 m were used directly, and the thermal infrared band was excluded. Twentieth-level Google Earth images from 2002 to 2017 with a spatial resolution of 0.27 m were selected for monitoring the Shunji Bridge and Shunji New Bridge. The time series images are shown in Figure 2.

### 2.3. Methods

A flowchart of the methods used in this study is shown in Figure 3.

In this study, dynamic remote sensing monitoring of the Shunji Bridge from environmental factors at the macroscale and the protected cultural site at the microscale was carried out. In terms of environmental factor monitoring, Landsat 7 ETM+ and Sentinel-2 images were used to extract various environmental factor information for the Jinjiang River Basin, including land cover information, vegetation cover information, topography information, and soil erosion information. In terms of monitoring the cultural relic, the time series images of high spatial resolution were used to extract area attribute information for the Shunji Bridge and the nearby bridge. Based on the dynamic monitoring results in the Jinjiang River Basin and the protected cultural site, the whole process of destruction was traced, and the causes of the Shunji Bridge destruction were analysed.

#### 2.3.1. Land Cover Classification

Five land cover classes were defined in the Jinjiang River Basin: artificial surface, barren land, farmland, vegetation and water. The characteristics of these land cover classes are listed in Table 3.

The classification and regression tree (CART) is a decision tree based on machine learning. The CART is generated by recursively constructing a binary decision tree. Commonly, the CART method outperforms maximum likelihood classification (MLC) and linear discriminant function classification, and the relatively simple, explicit, and intuitive classification structure is the most distinctive advantage of the CART method [52].

Landsat 7 ETM+ images in 2000 and Sentinel-2 images in 2019 were used for land cover classification. The CART method was performed in GEE to classify land cover classes in the Jinjiang River Basin for the two time periods separately, and the results were compared to extract the land cover change information.

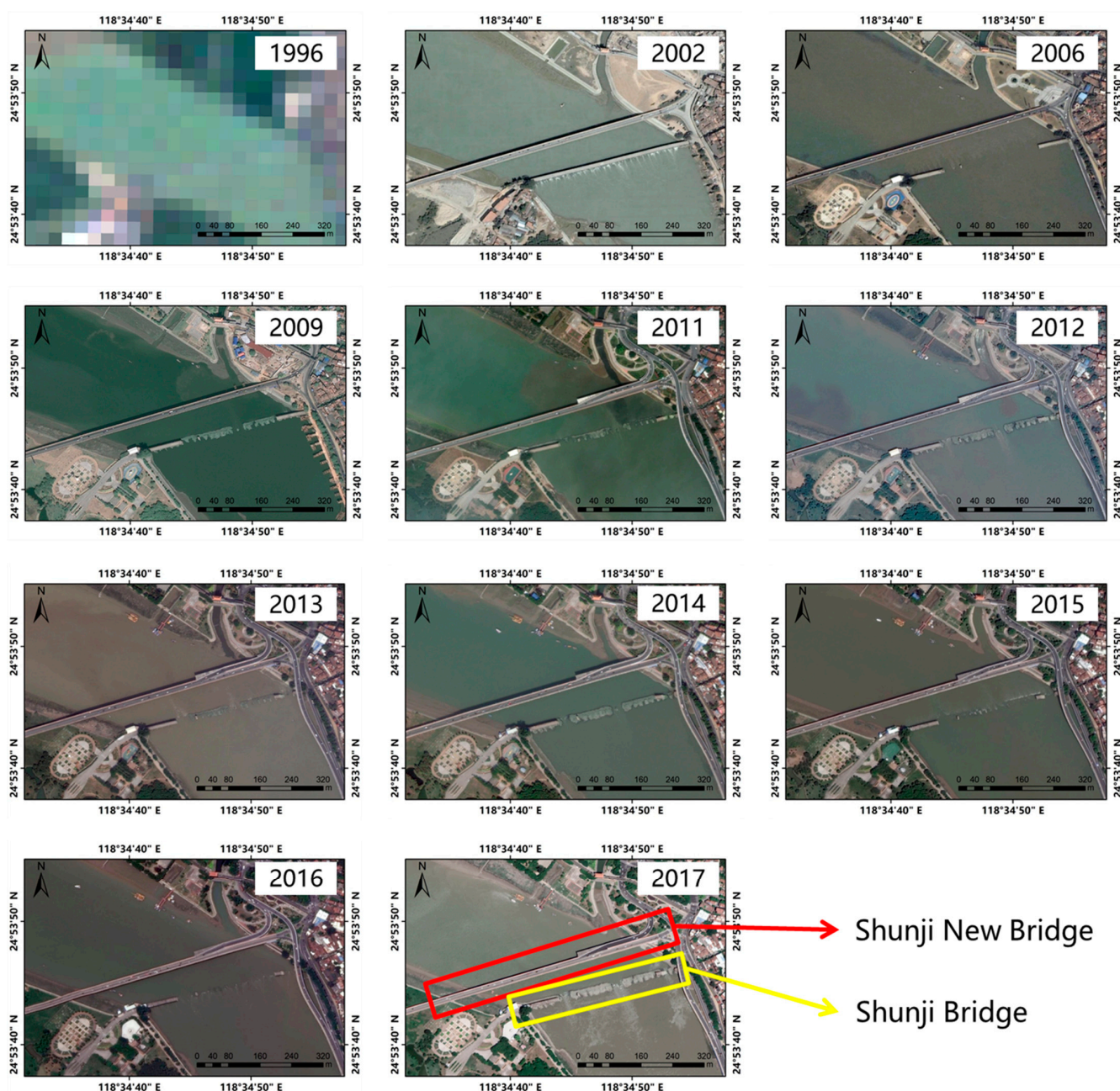


Figure 2. Time series images used for monitoring the protected cultural site.

Table 3. Land cover classification system in the Jinjiang River Basin.

Classification	Description of Characteristics
Artificial surface	Including residential, commercial, industry, public, traffic networks such as roads and bridges.
Barren land	Mainly including bare soil.
Farmland	Cultivable land.
Vegetation	Including woodland, grassland, shrubland and green belt in the urban areas.
Water	Including rivers, ponds, lakes and canals.

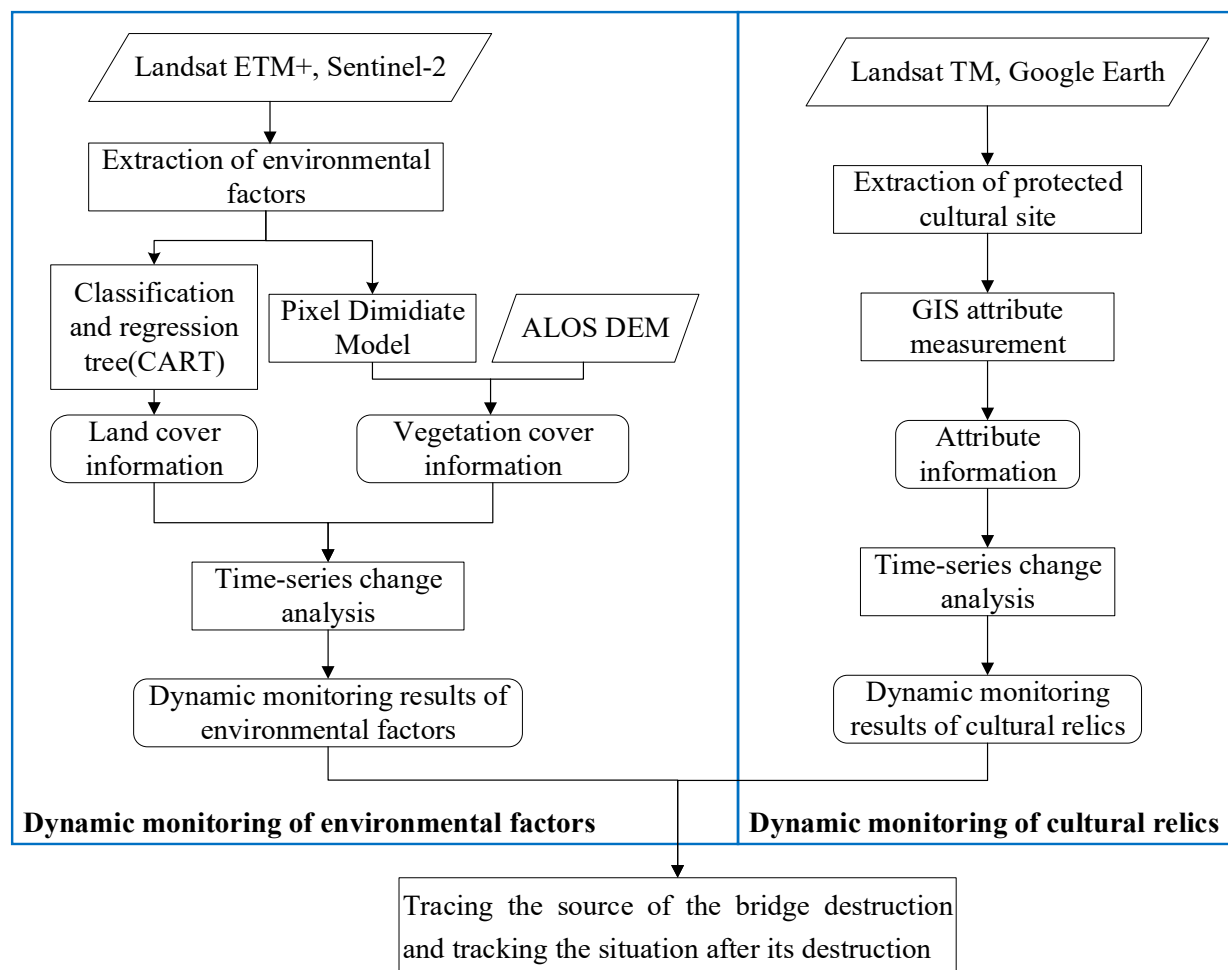


Figure 3. Flowchart for monitoring environmental factors and cultural relics.

### 2.3.2. Vegetation Cover Information

The NDVI can reflect the growth of vegetation. It is defined as the ratio of the reflectance difference between the near-infrared band and red band and the sum of the reflectance of these two bands. Thus, the NDVI values are normalized between  $-1$  and  $1$ . As a more intuitive index, the fractional vegetation cover (FVC) describes a vertical projection of the areal proportion of a landscape occupied by green vegetation [53] and can reflect the characteristics and changes in vegetation coverage. The FVC is derived from the NDVI as follows [54].

$$FVC = \frac{NDVI - NDVI_{soil}}{NDVI_{veg} - NDVI_{soil}} \quad (1)$$

where  $NDVI$ ,  $NDVI_{soil}$  and  $NDVI_{veg}$  indicate the NDVI value of any given pixel and the NDVI values of the bare soil and vegetation pixels, respectively.

In an ideal situation,  $NDVI_{soil}$  is zero, and  $NDVI_{veg}$  is one. However, due to complex conditions, such as ground humidity, soil type and vegetation type,  $NDVI_{soil}$  and  $NDVI_{veg}$  change over time and space. To define the values of  $NDVI_{soil}$  and  $NDVI_{veg}$ , the NDVI value for each pixel in the image was calculated first, and the cumulative probability distribution of the NDVI values was derived. A confidence level of 5% was chosen in this study, which means that  $NDVI_{soil}$  was defined as 5% of the cumulative probability of the NDVI values and that  $NDVI_{veg}$  was defined as 95% of the cumulative probability of the NDVI values [55]. This method decomposes the vegetation and bare soil information

from all the image pixels by the given thresholds and is thus called the pixel dimidiate model [56].

In GEE, Landsat 7 ETM+ images from 2000 and 2010 and Sentinel-2 images from 2019 were used to calculate the NDVI in the Jinjiang River Basin. Then, the FVC was calculated according to Formula (1). The FVC was used to analyse the spatial and temporal characteristics of vegetation coverage in the river basin.

### 2.3.3. Topographic Information

The slope of the landform is the tangent of the angle of that surface to the horizontal. A slope of zero indicates a horizontal surface, whereas a larger slope indicates a steep surface. In this study, the slope information was extracted from the DEM data. Since the vegetation cover types are closely related to topography, the vegetation cover types were analysed using zonal statistics based on different elevations and slopes.

### 2.3.4. Soil Erosion Information

The intensity of soil erosion can be inferred from the environmental factors. According to the standards of soil erosion classification and grading [57], the soil erosion intensity was classified and divided into five grades: mild, moderate, strong, extremely strong and severe. The classification and grading standards were based on the joint analysis of slope and vegetation coverage, as shown in Table 4. The year 2010 was chosen because it represents the time when the disaster occurred.

**Table 4.** The classification and grading standards of soil erosion in the Jinjiang River Basin.

FVC	Slope					
	0–5°	5–8°	8–15°	15–25°	25–35°	>35°
0.75–1.00	Mild	Mild	Mild	Mild	Mild	Mild
0.60–0.75	Mild	Mild	Mild	Mild	Mild	Moderate
0.45–0.60	Mild	Mild	Mild	Mild	Moderate	Strong
0.30–0.45	Mild	Mild	Mild	Moderate	Strong	Extremely strong
0.00–0.30	Mild	Mild	Moderate	Strong	Extremely strong	Severe

### 2.3.5. Attribute Measurement

The varying area percentages of the Shunji Bridge and Shunji New Bridge were measured to obtain attribute information for these two bridges from the time series images. The spatial and temporal changes in the area percentages of the two bridges were extracted and analysed.

## 3. Results

### 3.1. Results of Land Cover Classes

The classification results for the Jinjiang River Basin for 2000 and 2019 are shown in Figure 4. The classification results were verified on selected testing data. The overall accuracies of the classification results were 96.25% for 2000 and 88.75% for 2019.

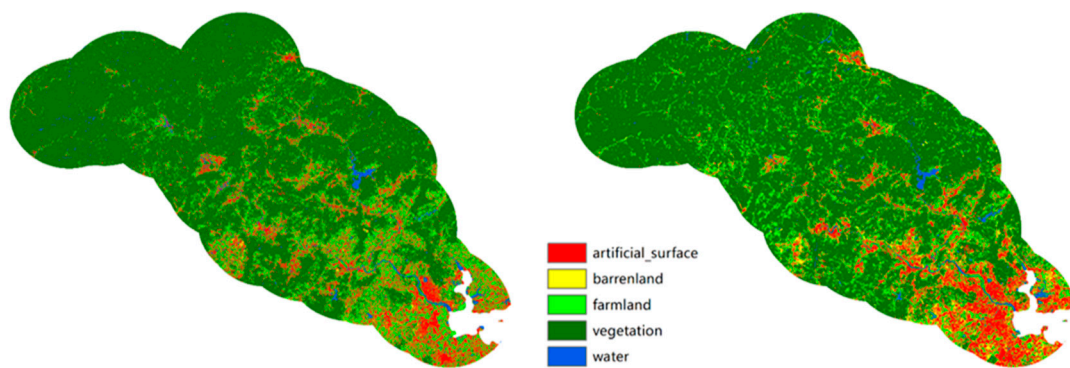


**Figure 4.** Land cover classification results for the Jinjiang River Basin for 2000 (left) and 2019 (right).

The upper reaches of the Jinjiang River Basin are mountainous, and vegetation is the main land cover class, as shown in Figure 4. There is a large portion of farmland in the middle reaches of the river. The lower reaches of the river are located in the coastal plain, which has a high level of urbanization. In this area, the main land cover class is artificial surface. Most barren land is distributed in the lower reaches of the river due to urban construction. Small areas of barren land are sparsely distributed in the upper reaches and are mainly caused by deforestation.

The most distinct changes in the whole basin between 2000 and 2019 were the decrease in the farmland class and the increase in the artificial surface class. The areas of the land cover classes were calculated for 2000 and 2019 and are shown in Figure 5.

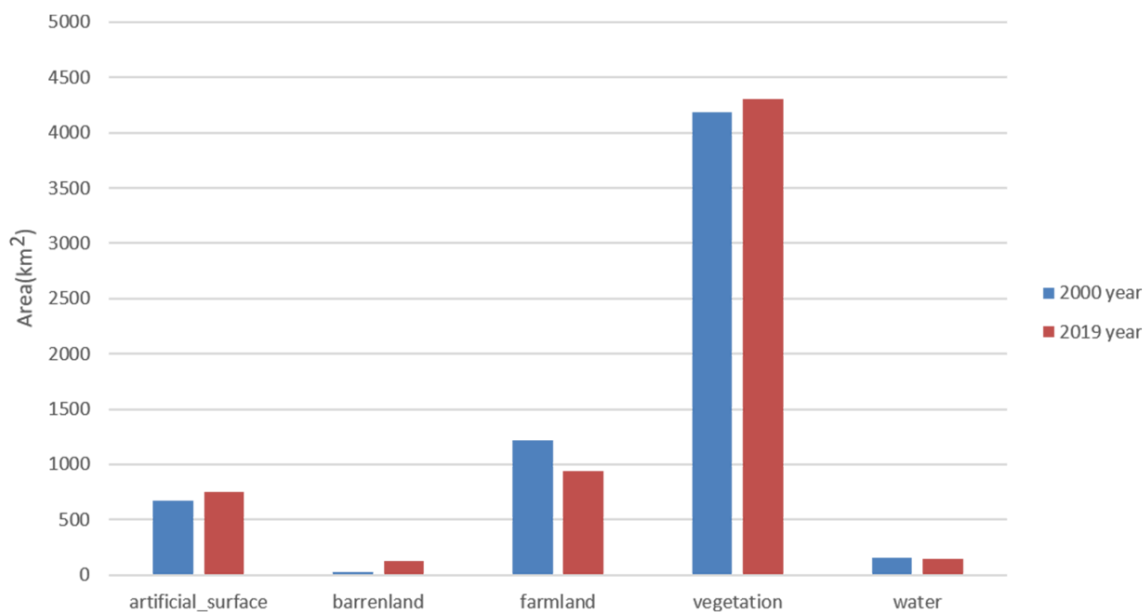


**Figure 5.** Column chart of the areas of the land cover classes for 2000 and 2019 in the Jinjiang River Basin (km<sup>2</sup>).

According to Figure 5, the area of the farmland class decreased by 271.95 km<sup>2</sup> from 2000 to 2019, accounting for 4.35% of the total area. The areas of artificial surface, barren land and vegetation classes increased by 75.77 km<sup>2</sup>, 92.84 km<sup>2</sup> and 120.18 km<sup>2</sup>, respectively. The increasing proportions were 1.21%, 1.48% and 1.92% for these three classes. The area of the water class barely changed.

This conversion indicates that urbanization occurred over the 19 years. Specifically, in the lower reaches of the Jinjiang River in the south-eastern part of the basin area where the Shunji Bridge was located, the artificial surface areas increased sharply, and the farmland areas decreased, indicating that urbanization caused a loss of farmland. This local trend is consistent with the global trend in the Jinjiang River Basin.

### 3.2. Results of Vegetation Cover

To show the different degrees of vegetation coverage, the FVC values were divided into five grades: extremely low coverage (0.0–0.2), low coverage (0.2–0.4), middle coverage (0.4–0.6), middle high coverage (0.6–0.8), and high coverage (0.8–1.0) [58]. The FVC grade distributions in the Jinjiang River Basin for 2000, 2010 and 2019 are shown in Figure 6. The vegetation coverage of the basin obviously improved; in particular, the area of high vegetation coverage continuously increased from 2000 to 2010 and from 2010 to 2019.

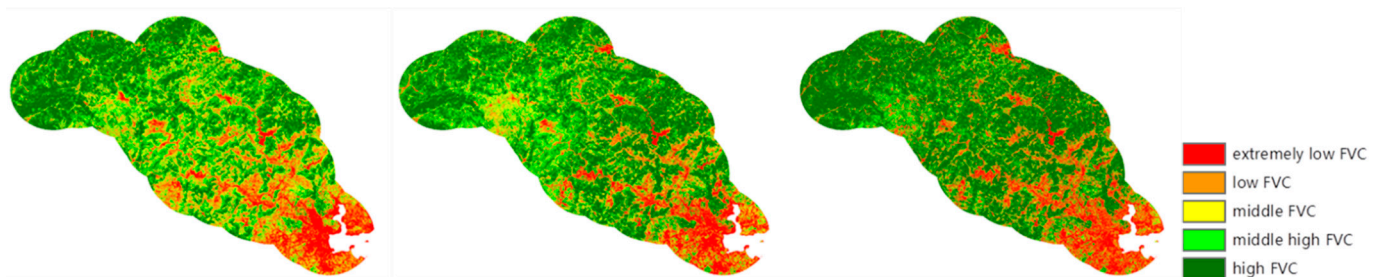


**Figure 6.** FVC grading results in the Jinjiang River Basin for 2000 (left), 2010 (middle) and 2019 (right).

The average FVC value in the upper reaches of the Jinjiang River increased from 0.72 to 0.73 between 2000 and 2010 and from 0.73 to 0.78 between 2010 and 2019. In the middle reaches, the average FVC value increased from 0.56 to 0.66 between 2000 and 2010 and from 0.66 to 0.67 between 2010 and 2019. In the lower reaches, the average FVC value increased from 0.25 to 0.29 between 2000 and 2010 and from 0.29 to 0.30 between 2010 and 2019. The average FVC value was the highest in the upper reaches and the lowest in the lower reaches. From 2000 to 2010, the average FVC values greatly increased in the middle and lower reaches. From 2010 to 2019, the vegetation coverage in the upper reaches greatly increased.

The area of each FVC grade was calculated for 2000, 2010 and 2019. The column chart of the areas of the FVC grades is shown in Figure 7 for the three years.

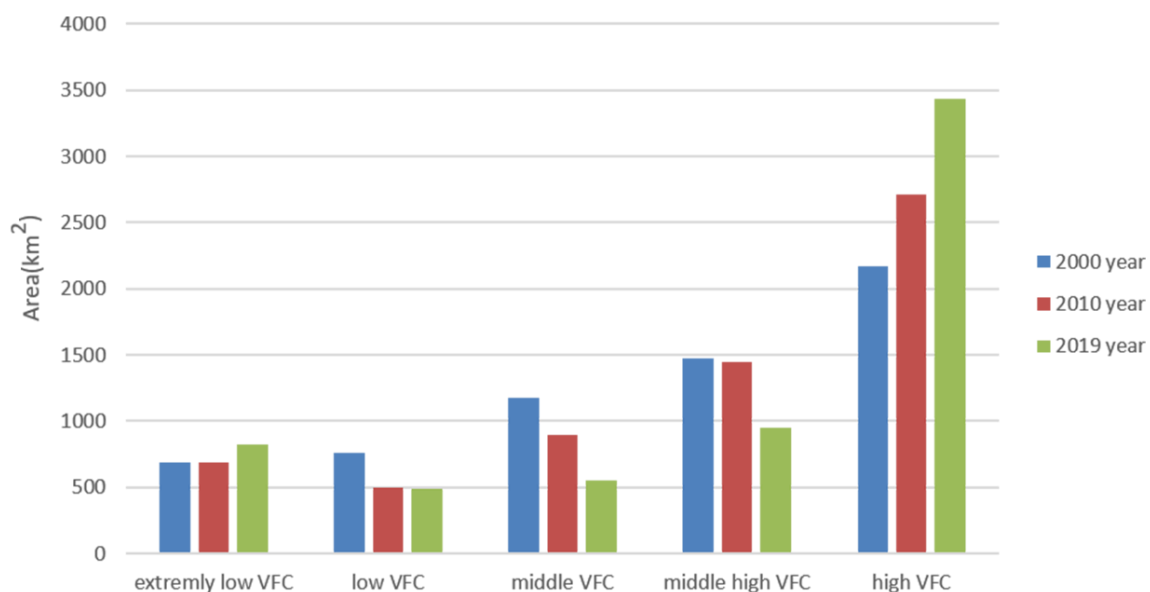


**Figure 7.** Column chart of the areas of the FVC grades in the Jinjiang River Basin for 2000, 2010 and 2019 (km<sup>2</sup>).

As shown in Figure 7, from 2000 to 2019, the areas with extremely low FVC increased from 689.63 km<sup>2</sup> to 826.00 km<sup>2</sup>, with a total increase of 136.37 km<sup>2</sup>. The area with high FVC increased from 2165.81 km<sup>2</sup> to 3438.75 km<sup>2</sup>, with a total increase of 1272.94 km<sup>2</sup>. The increased proportions were 2.18% and 20.34% for extremely low FVC and high FVC,

respectively. However, the area with low FVC decreased from 758.14 km<sup>2</sup> to 448.11 km<sup>2</sup>, with a total decrease of 270.03 km<sup>2</sup>. The area with middle high FVC decreased from 1469.89 km<sup>2</sup> to 950.26 km<sup>2</sup>, with a total decrease of 519.62 km<sup>2</sup>. The area with middle FVC decreased from 1175.56 km<sup>2</sup> to 556.16 km<sup>2</sup>, with a total decrease of 619.40 km<sup>2</sup>. The decreased proportions accounted for 4.31%, 8.30% and 9.90% for low FVC, middle-high FVC and middle FVC, respectively.

The average FVC value in the basin increased from 0.62 to 0.66 between 2000 and 2010 and from 0.66 to 0.69 between 2010 and 2019, showing a promising increasing trend in the FVC. In particular, the areas with high vegetation coverage and areas with extremely low vegetation coverage both increased, with the former increasing 18.15% more than the latter. This result indicates that the vegetation coverage in the Jinjiang River Basin increased overall. In the lower reaches of the Jinjiang River, trees and grass were planted for urban greening during the urbanization of the area surrounding the Shunji Bridge. The local trend also shows increased vegetation coverage.

### 3.3. Results of Topography

The ALOS DEM and slope data in the Jinjiang River Basin are shown in Figure 8.

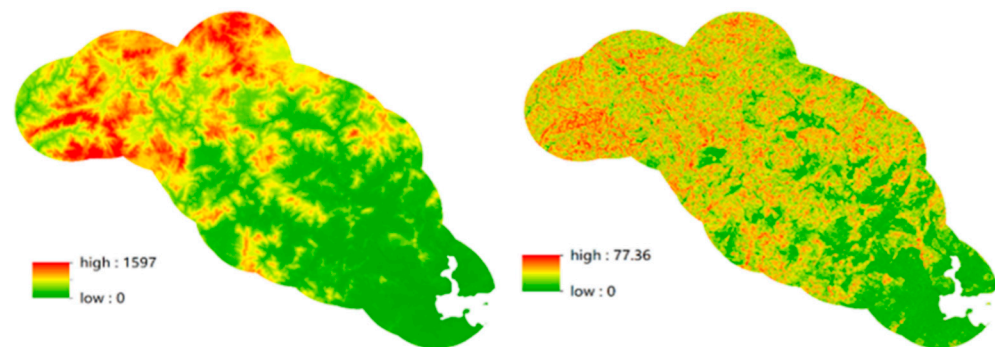


**Figure 8.** DEM (left) and slope (right) in the Jinjiang River Basin in 2007.

The terrain gradually decreases from the northwest to the southeast in the Jinjiang River Basin. The mountainous area in the upper reaches of the Jinjiang River is high, steep and rugged, and the plains area in the lower reaches is low and rather flat. In the basin area, the highest elevation is 1597 m, and the average elevation is 408.5 m. The steepest slope is 77.36°, and the average slope is 16.04°. The average elevation in the upper reaches of the Jinjiang River is 571.86 m, and the average slope is 19.34°. The average elevation in the middle reaches is 220.85 m, and the average slope is 13.85°. The average elevation in the lower reaches is 40.77 m, and the average slope is 5.44°. The elevation and slope in the river basin gradually decrease from the upper reaches to the lower reaches.

Considering that FVC has a close connection with topography, the FVC was analysed using zonal statistics based on different groups of elevations. The DEM data were divided into groups at an interval of 100 m. The changes in the FVC with elevation are shown in Figure 9.

As revealed by Figure 9, the FVC increases as the elevation increases in the elevation ranges from 0 to 300 m and 500 m to 1200 m, while it decreases in the elevation ranges from 300 m to 500 m and 1200 m to 1597 m. In the area with elevations lower than 100 m, the FVC value is rather low (less than 0.5) because this area is located in the lower reaches of the Jinjiang River, which has a high level of urbanization. The vegetation coverage is mainly from urban vegetation rather than forests; thus, the FVC is low. In the area with elevations higher than 1200 m, the FVC value significantly decreases as the elevation increases. This area is located in the upper reaches of the Jinjiang River, and vertical belts of vegetation are clear in this mountainous area. As the elevation increases, the temperature decreases, and the vegetation coverage decreases.

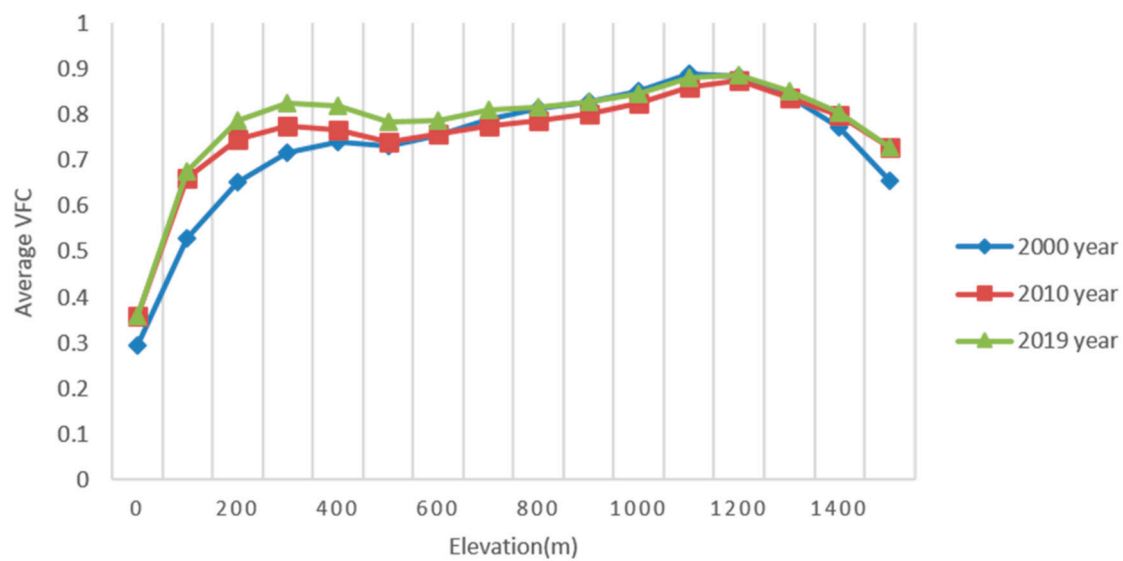


**Figure 9.** The changes in the FVC with elevation in the Jinjiang River Basin for 2000, 2010, and 2019.

Similar to elevation, the FVC was also analysed using zonal statistics based on different groups of slopes. The slope product was divided into groups at an interval of  $5^\circ$ . The changes in the FVC with slope are shown in Figure 10.

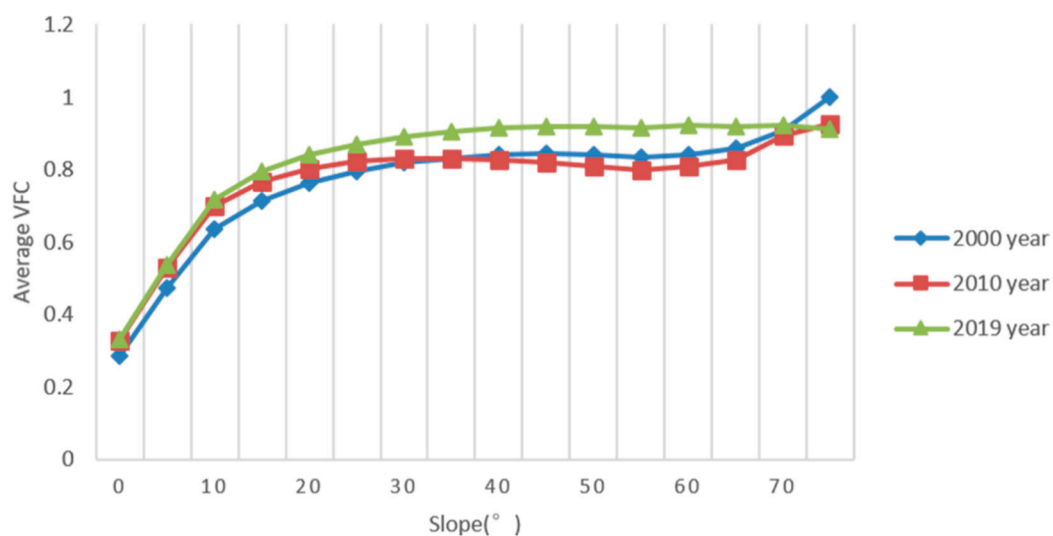


**Figure 10.** The changes in the FVC with slope in the Jinjiang River Basin for 2000, 2010, and 2019.

The FVC increases as the slope increases over the whole slope range. Specifically, in areas with slopes less than  $10^\circ$ , the FVC value is low (less than 0.6). The same reason causes the low vegetation coverage in the urban area in the lower reaches of the Jinjiang River. The Shunji Bridge is located in this area, with an elevation below 300 m and a slope of less than  $10^\circ$ . The area surrounding the Shunji Bridge has low vegetation coverage due to the high level of urbanization, as shown in Figures 9 and 10.

### 3.4. Results of Soil Erosion

From the above results, it can be inferred that the collapse of the Shunji Bridge was partly related to the inhospitable environment of the Jinjiang River Basin. According to grades in Table 4, the spatial distribution of soil erosion intensity in the Jinjiang River Basin is produced in Figure 11.

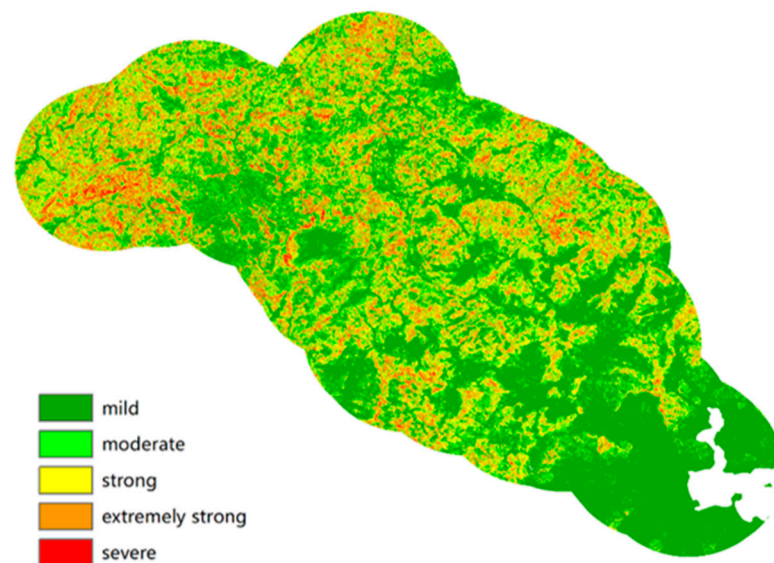


**Figure 11.** The soil erosion intensity in the Jinjiang River Basin.

As shown in Figure 11, the area of soil erosion intensity above moderate is 2512.90 km<sup>2</sup>, accounting for 40.16% of the basin. Severe soil erosion is mainly distributed in the upper and middle reaches because of the degradation of forests and farmland. The lower reaches of the Jinjiang River are urban areas with low vegetation coverage. Such an environment is vulnerable to natural disasters such as typhoons and floods. As a consequence, when rainstorms occurred, floods from the upper and middle reaches of the Jinjiang River posed a serious threat to the Shunji Bridge in the lower reaches.

### 3.5. Results of Attribute Information

The time series images, including Landsat 5 TM and high spatial resolution Google Earth images of the protected cultural site Shunji Bridge, is shown in Figure 11. The Shunji Bridge is marked in yellow, and the Shunji New Bridge is marked in red.

As shown in Figure 12, the Shunji New Bridge had not yet been built in 1996. In 2002, the Shunji New Bridge had been built, and the Shunji Bridge had not yet been damaged. In 2006, the Shunji Bridge collapsed for the first time. It has remained as a broken bridge since then. In 2011, a section was added to the north of the Shunji New Bridge, and the Shunji Bridge collapsed for the second time. There were no obvious changes in the two bridges after that.

The area percentages of the two bridges were measured from the time series images. A line chart showing the changes in the area percentages is shown in Figure 13.

As shown in Figure 13, the area percentage of the Shunji Bridge did not change before 2006. In 2006, the Shunji Bridge collapsed for the first time, and the area percentage decreased by 57%. In 2011, the area percentage of the Shunji New Bridge increased by 21% after the construction of a new bridge section. The Shunji Bridge collapsed again, and the area percentage decreased by 6%. Since then, the areas of the two bridges have not changed.

From the above results, we hypothesized that the collapse of the Shunji Bridge was related to the construction of the Shunji New Bridge. The construction of the Shunji New Bridge blocked water to some degree and compromised the original balance of the river section, causing changes in the water velocity and sediment movement.

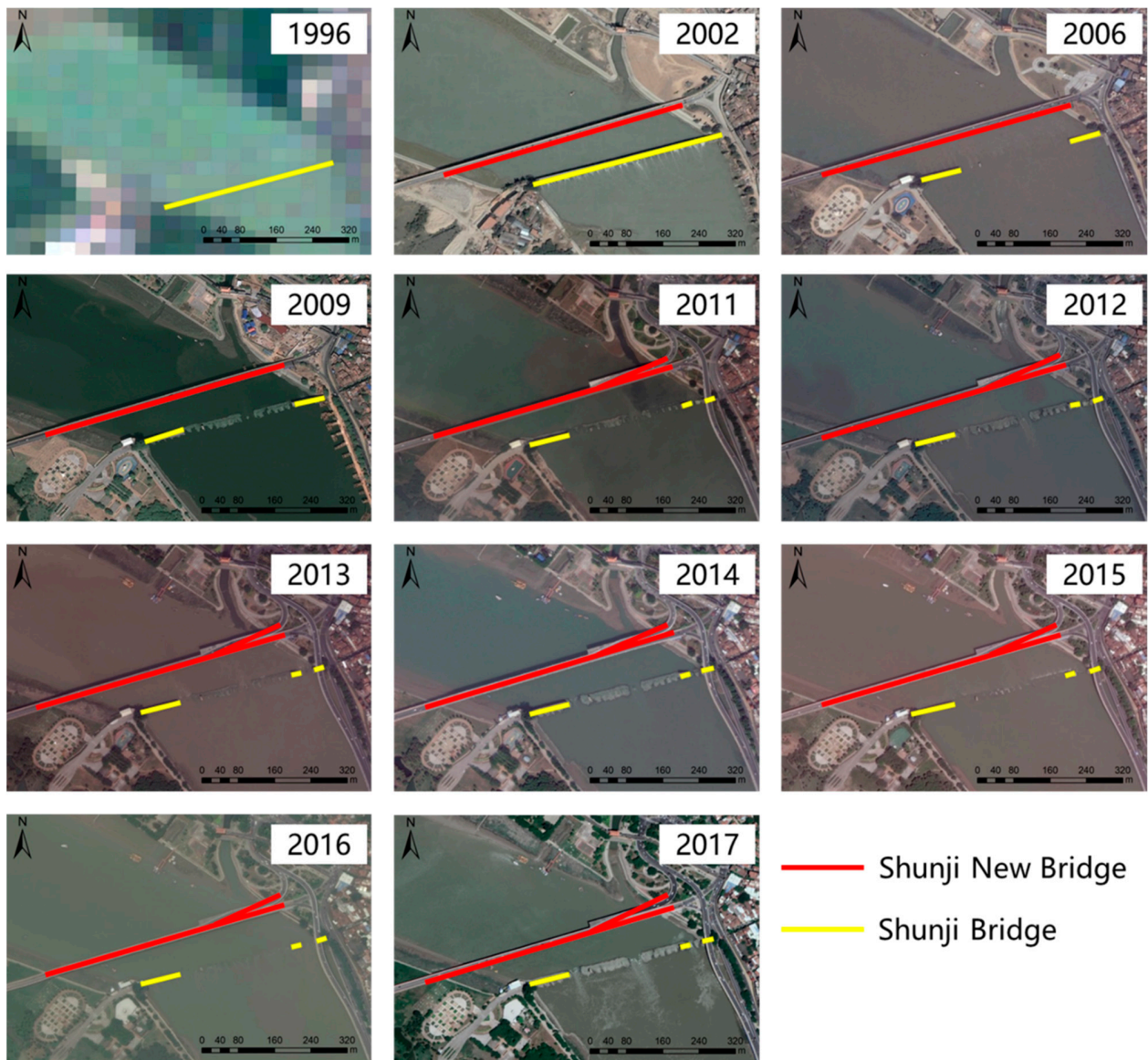


Figure 12. Time series images of the Shunji Bridge and Shunji New Bridge.

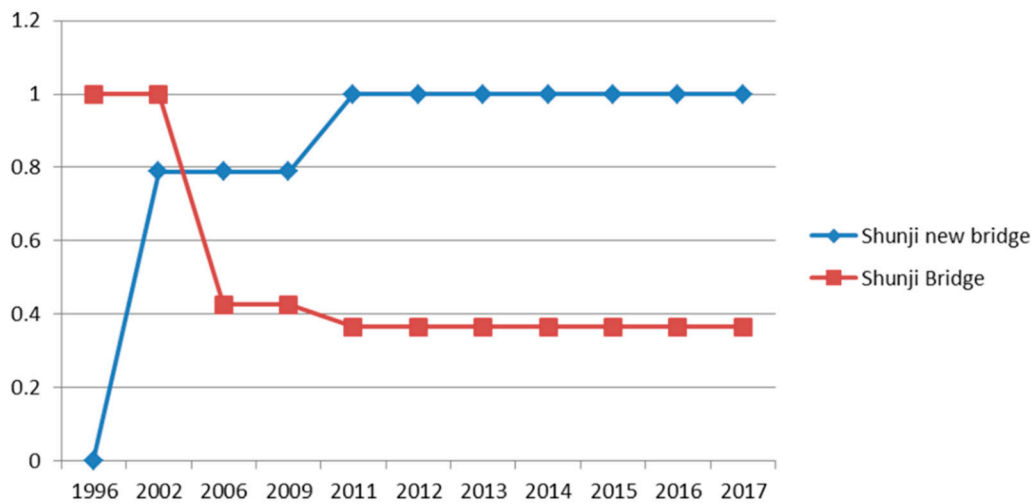


Figure 13. Line chart showing the changes in the area percentages of the Shunji Bridge and Shunji New Bridge from 1996 to 2017.

## 4. Discussion

### 4.1. Evaluation of Impact Factors

To evaluate the impact degree of each factor on immovable cultural relics, this study uses the analytic hierarchy process (AHP) to establish an index evaluation system. The AHP was proposed by Saaty in the 1970s. The idea of this method is to sort index according to its importance and decide the weight of each index [59].

The steps for AHP include (1) defining the problem and determining the goal; (2) developing the hierarchy structure and establishing an index evaluation system; (3) applying a comparison matrix for each index; (4) conducting the consistency check; (5) determining the relative weight of each index [60]. It is generally agreed that the consistency ratio (CR) < 0.1 leads to a satisfactory consistency.

In this study, the impact factors include land cover, vegetation cover, topography, soil erosion and the Shunji New Bridge. Therefore, an index evaluation system was established according to these five impact factors, experts were invited to score these factors, and the comparison matrix U was derived as follows.

$$U = \begin{bmatrix} 1 & 3 & 4 & 1 & 1 \\ \frac{1}{3} & 1 & 3 & \frac{1}{3} & \frac{1}{2} \\ \frac{1}{4} & \frac{1}{3} & 1 & \frac{1}{4} & \frac{1}{3} \\ 1 & 3 & 4 & 1 & \frac{1}{2} \\ 1 & 2 & 3 & 2 & 1 \end{bmatrix} \quad (2)$$

The five elements from left to right and from top to bottom represent land cover, vegetation cover, topography, soil erosion and the Shunji New Bridge, respectively. The number "1" means two factors contribute equally to the objective, "2" means one factor is slightly favour over another, "3" means one factor is strongly favour over another, and "4" means one factor is very strongly favour over another.

The weight of each index was calculated by obtaining the eigenvector of the comparison matrix. The derived eigenvector is  $W = (0.2766, 0.1220, 0.0640, 0.2478, 0.2887)^T$ , and the CR = 0.016. Since the CR is less than 0.1, it indicates a good consistency. Therefore, the Shunji New Bridge has the greatest impact, followed by land cover and soil erosion. The impacts of vegetation cover and topography on the Shunji Bridge are relatively small, mainly because vegetation cover is directly affected by land cover, and topography is an attribute that does not constantly change.

This study monitored the impact factors related to the damage of the Shunji Bridge, including the environmental factors and the bridge's attribute. However, some other impact factors cannot be obtained by remote sensing techniques, such as rainfall, wind direction, sunshine time, and the materials and structure of the bridge. These factors also have important impacts on the damage of the bridge and can be obtained by other technical means and data sources. Since we did not monitor all of the impact factors, the extracted five factors partly contributed to the bridge's destruction. Nevertheless, this study has demonstrated a fair example of some impact factors that can be derived from remote sensing techniques.

### 4.2. Efficiency in GEE

The experiment was performed on the GEE to extract environmental factors from Landsat 7 ETM+ and Sentinel-2 images. To demonstrate the high efficiency of the GEE platform, the computational costs and random-access memory (RAM) of the process were implemented in the GEE platform and the traditional software (i.e., ENVI and SNAP), respectively, for comparison. All procedures were performed on a Lenovo laptop with an Intel (R) Core (TM) i5-7300HQ CPU processor and a Windows 10 64-bit operating system. The computational costs and RAM are shown in Tables 5 and 6.

**Table 5.** Computational and RAM costs of the data process in GEE and ENVI for Landsat 7 ETM+ images.

		Data	Gapfill	Atmospheric Correction	Mosaic	Subset	Classification and NDVI Information Extraction
Time	ENVI	2.5 h	4 h	18 h	20 h	0.4 h	1.8 h
	GEE	The total time is approximately 0.26 h.					
RAM	ENVI	5.6 GB	4.9 GB	5.1 GB	5.2 GB	3.3 GB	0.64 GB
	GEE	0					

**Table 6.** Computational and RAM costs of the data process in GEE and SNAP for Sentinel-2 images.

		Data	Resampling	Mosaic	Subset	Classification and NDVI Information Extraction
Time	SNAP	3.5 h	12 h	15 h	4 h	2.4 h
	GEE	The total time is approximately 0.29 h.				
RAM	SNAP	5.1 GB	43.2 GB	43.1 GB	35.6 GB	1.21 GB
	GEE	0				

From the efficiency comparison of the different software, it can be seen that data processing on the GEE platform can save considerable time and RAM. It is therefore suggested that GEE is worthy of promotion in many applications.

## 5. Findings

In this paper, the Shunji Bridge, from environmental factors at the macroscale to the protected cultural site at the microscale, was studied using remote sensing techniques. The causes related to the damage of the Shunji Bridge were analysed from multiple aspects. At the macroscale, Landsat series and Sentinel-2 images were processed in the GEE platform to extract multiple environmental factors. According to the dynamic monitoring results derived from environmental factors, the urbanization process in the Jinjiang River Basin has accelerated. The vegetation coverage in this area also increased. At the microscale, Google Earth time series images were used to extract attribute information of the cultural relic, and the spatial and temporal changes in the Shunji Bridge before and after the destruction were detected. The causes of its destruction were analysed quantitatively. The results show that construction activities greatly affected the Shunji Bridge. Although some other factors may also contribute to the destruction of the bridge, this study has shown the practicability of monitoring the changes of cultural relics in the hazard and tracing the causes of the bridge's destruction using remote sensing. The findings of this study are as follows.

In terms of the source of the destruction of the Shunji Bridge, the rainstorm caused by typhoons in July 2006 was the initial trigger for this disaster. However, both the surrounding environment and the construction of the Shunji New Bridge contributed to the destruction of this cultural relic. On the one hand, there was a large area of barren land in the upper reaches of the Jinjiang River because of the deforestation and farmland degradation, causing serious water loss and soil erosion. On the other hand, the Shunji New Bridge, located 80 m upriver, blocked water to some degree, leading to sedimentation near the Shunji Bridge. The inhospitable surrounding environment and long-term sedimentation in the river were potential threats to the Shunji Bridge. When the rainstorms occurred, the river water rose rapidly, and the flood water could not drain downstream in time due to sedimentation. The rainstorms brought branches and silt that hit the Shunji Bridge. Finally, the Shunji Bridge collapsed, and the damage was irreversible.

By tracking the situation after destruction, urbanization and greening in the Jinjiang River Basin have continued. Since urbanization has a great impact on immovable cultural

relics, urban construction should be avoided as much as possible in the areas surrounding immovable cultural relics. Moreover, urban construction should be reasonably planned before implementation, and urban greening should be further improved.

## 6. Conclusions

“Strengthening efforts to protect and safeguard the world’s cultural and natural heritage” is one of the targets (Target 11.4) of the United Nations Sustainable Development Goals (SDGs). This study has shown the advantages of remote sensing and GIS techniques for cultural heritage monitoring and protection planning. According to this case study of the Shunji Bridge, the findings can provide guidance and suggestions for the protection of immovable cultural relics in regional urban planning and construction, as well as technical support for regional natural disaster risk assessment. The emergency response and preventive protection of immovable cultural relics can be enhanced by environmental change and early warning monitoring. Moreover, it is important to publicize this information and provide a better perspective to all people. For example, a special day, such as the “Cultural and Natural Heritage Day”, could be established, and educational activities could be held to raise public awareness of cultural heritage protection.

The methods used in this study are also applicable to other types of cultural heritage. Due to the small scale of the Shunji Bridge, only the area property of the cultural site was extracted. However, when studying ancient buildings and ancient sites with large areas, other information of cultural heritages can be extracted and analysed, such as vegetation and buildings around the cultural landscapes. Dynamic remote sensing-based monitoring can be performed on the surrounding environments of protected cultural sites to extract change information, so that the impacts of natural and human factors on cultural heritage can be obtained.

In the future, observed satellite data and remote sensing techniques are expected to be further improved to better serve the cultural heritage protection. In terms of data, for example, the Planet satellite provides images with a spatial resolution of 3–5 m and can achieve daily coverage at the global scale. The recently launched satellite, SuperDove, obtains the images with a spatial resolution of 3 m and 8 multispectral bands. The Planet and SuperDove images can be used to monitor large-scale cultural sites, such as ancient buildings and ancient sites. The rich spectral information lies in images with eight multispectral bands and has the potential to monitor different types of tree species in natural heritage sites. However, to monitor small relics, such as bridges and towers, the images with a sub-meter spatial resolution are required. The current available sub-meter images, such as Pleiades and WorldView, do not have a very high temporal resolution. Therefore, cultural heritage protection can be promoted with the development of remote sensing satellites.

In terms of techniques, information extraction is the core of the dynamic monitoring process. Either in traditional software or the GEE platform, the selection of samples is required for land cover classification. This procedure is time consuming and laborious. More importantly, the experts’ knowledge included in the sample and feature selections could be the biggest obstacle for the non-remote-sensing researchers. The deep learning technique provides an automatic approach for extracting information. However, this type of approach is easily affected by many factors, such as weather conditions, acquisition time, solar azimuth, etc. For atypical buildings, such as heritage sites, the accuracy derived by the automatic information extraction approach has not reached the requirements for practical use. Therefore, the development of information extraction techniques is also important to accurately monitor cultural relics.

In summary, the research development trends in the protection of cultural heritages using remote sensing technology have the following aspects. First, with the development of unmanned aerial remote sensing systems (UARSSs), LiDAR technology and hyperspectral remote sensing, more data will be available for monitoring cultural heritage, and these data should be comprehensively utilized. Accordingly, the data processing techniques

should be further improved. Some tools that can deal with massive amounts of data, such as the GEE platform, should be popularized among non-remote-sensing experts. Second, it is suggested that change detection should be updated annually within the core and buffer zones of each protected cultural site. The changes in some key factors, such as vegetation and buildings, can be monitored so that experts can evaluate whether these changes pose threats to the cultural relics. Finally, we traced the source of a relic's destruction and tracked the situation after its destruction. With the improvement in the spatial and temporal resolution of satellite images, it will be possible to conduct the long-term monitoring of important cultural relics with potential safety hazards. By doing so, disasters may be detected in advance, and emergency responses can be taken to prevent damage. These measures are important for reducing the disaster risks of cultural relics and strengthening preventative protection.

**Author Contributions:** Software, Y.L.; writing—original draft preparation, Y.L.; data curation, Y.L. and Y.T.; visualization, Y.L. and Y.T.; investigation, Y.L. and F.C.; methodology, Y.T.; funding acquisition, L.J. and F.C.; conceptualization, F.C.; project administration, F.C.; supervision, L.J., F.C. and P.W. All authors have read and agreed to the published version of the manuscript.

**Funding:** This research was funded by the National Key R&D Program of China (No. 2019YFC1520800); the Aerospace Information Research Institute, Chinese Academy of Sciences (Y951150Z2F); and the National Natural Science Foundation of China (41972308, 42071312).

**Institutional Review Board Statement:** Not applicable.

**Informed Consent Statement:** Not applicable.

**Data Availability Statement:** Not applicable.

**Acknowledgments:** The authors thank the Key Laboratory of Digital Earth Science for supporting this research with the hardware device, and the three anonymous reviewers and the Academic Editor for providing helpful comments and suggestions to improve the manuscript.

**Conflicts of Interest:** The authors declare no conflict of interest.

## References

1. Wang, J. Flood risk maps to cultural heritage: Measures and process. *J. Cult. Herit.* **2015**, *16*, 210–220. [[CrossRef](#)]
2. Li, H.; Zhang, J.; Sun, J.; Wang, J. A visual analytics approach for flood risk analysis and decision-making in cultural heritage. *J. Vis. Lang. Comput.* **2017**, *41*, 89–99. [[CrossRef](#)]
3. Haddad, N.A.; Fakhoury, L.A.; Sakr, Y.M. A Critical anthology of international charters, conventions & principles on documentation of cultural heritage for conservation, monitoring & management. *Mediterr. Archaeol. Archaeom.* **2021**, *21*, 291–310.
4. Stovel, H. *Risk Preparedness: A Management Manual for World Cultural Heritage*; ICCROM: Rome, Italy, 1998; pp. 1–16.
5. Mckercher, B.; Ho, P.S.Y.; Cros, H.D. Relationship between tourism and cultural heritage management: Evidence from Hong Kong. *Tour. Manag.* **2005**, *26*, 539–548. [[CrossRef](#)]
6. Sabbioni, C.; Cassar, M.; Brimblecombe, P.; Tidblad, J.; Drdacky, M. Global climate change impact on built heritage and cultural landscapes. *Int. Conf. Herit. Weather. Conserv.* **2006**, *1*, 395–401.
7. Hamilton, R.; Kucera, V.; Tidblad, J.; Watt, J. *The Effects of Air Pollution on Cultural Heritage*; Springer: New York, NY, USA, 2009.
8. Li, G.S.; Wang, W.F.; Qu, J.J.; Song, M.H. Study on temperature and humidity environment of grotto 72 at the Mogao Grottoes in Dunhuang, China. *Int. J. Climatol.* **2013**, *33*, 1863–1872. [[CrossRef](#)]
9. Ortiz, R.; Ortiz, P.; Martín, J.M.; Vázquez, M.A. A new approach to the assessment of flooding and dampness hazards in cultural heritage, applied to the historic centre of Seville (Spain). *Sci. Total Environ.* **2016**, *1*, 546–555. [[CrossRef](#)] [[PubMed](#)]
10. Forino, G.; Mackee, J.; Meding, J.V. A proposed assessment index for climate change-related risk for cultural heritage protection in Newcastle (Australia). *Int. J. Disaster Risk Reduct.* **2016**, *19*, 235–248. [[CrossRef](#)]
11. Oikonomopoulou, E.; Delegou, E.T.; Sayas, J.; Moropoulou, A. An innovative approach to the protection of cultural heritage: The case of cultural routes in Chios Island, Greece. *J. Archaeol. Sci. Rep.* **2017**, *14*, 742–757. [[CrossRef](#)]
12. Andretta, M.; Coppola, F.; Modelli, A.; Santopuoli, N.; Seccia, L. Proposal for a new environmental risk assessment methodology in cultural heritage protection. *J. Cult. Herit.* **2017**, *23*, 22–32. [[CrossRef](#)]
13. Figueiredo, R.; Romo, X.; Paupério, E. Flood risk assessment of cultural heritage at large spatial scales: Framework and application to mainland Portugal. *J. Cult. Herit.* **2020**, *43*, 163–174. [[CrossRef](#)]
14. Luo, L.; Wang, X.; Guo, H.; Lasaponara, R.; Zong, X.; Masini, N.; Wang, G.; Shi, P.; Khatteli, H.; Chen, F.; et al. Airborne and spaceborne remote sensing for archaeological and cultural heritage applications: A review of the century (1907–2017). *Remote Sens. Environ.* **2019**, *232*, 232. [[CrossRef](#)]

15. Lasaponara, R.; Masini, N. *Satellite Remote Sensing: A New Tool for Archaeology*; Springer: Heidelberg, Germany, 2012.
16. Agapiou, A.; Lysandrou, V. Remote sensing archaeology: Tracking and mapping evolution in European scientific literature from 1999 to 2015. *J. Archaeol. Sci. Rep.* **2015**, *4*, 192–200. [[CrossRef](#)]
17. Morehart, C.T.; Millhauser, J.K. Monitoring cultural landscapes from space: Evaluating archaeological sites in the Basin of Mexico using very high resolution satellite imagery. *J. Archaeol. Sci. Rep.* **2016**, *10*, 363–376. [[CrossRef](#)]
18. Luo, L.; Wang, X.; Lasaponara, R.; Xiang, B.; Zhen, J.; Zhu, L.; Yang, R.; Liu, D.; Liu, C. Auto-extraction of linear archaeological traces of Tuntian Irrigation Canals in Miran Site (China) from Gaofen-1 satellite imagery. *Remote Sens.* **2018**, *10*, 718. [[CrossRef](#)]
19. Lopes, A.S.; Macedo, D.V.; Brito, A.; Furtado, V. Assessment of urban cultural-heritage protection zones using a co-visibility-analysis tool. *Comput. Environ. Urban Syst.* **2019**, *76*, 139–149. [[CrossRef](#)]
20. Choi, Y.; Yang, Y.J.; Sohn, H.G. Resilient cultural heritage through digital cultural heritage cube: Two cases in South Korea. *J. Cult. Herit.* **2021**, *48*, 36–44. [[CrossRef](#)]
21. Dupont, L.; Eetvelde, V.V. Assessing the potential impacts of climate change on traditional landscapes and their heritage values on the local level: Case studies in the Dender basin in Flanders, Belgium. *Land Use Policy* **2013**, *35*, 179–191. [[CrossRef](#)]
22. Moropoulou, A.; Labropoulos, K.C.; Delegou, E.T.; Karoglou, M.; Bakolas, A. Non-destructive techniques as a tool for the protection of built cultural heritage. *Constr. Build. Mater.* **2013**, *48*, 1222–1239. [[CrossRef](#)]
23. Cerra, D.; Agapiou, A.; Cavalli, R.M.; Sarris, A. An objective assessment of hyperspectral indicators for the detection of buried archaeological relics. *Remote Sens.* **2018**, *10*, 500. [[CrossRef](#)]
24. Banerjee, R.; Srivastava, P.K. Reconstruction of contested landscape: Detecting land cover transformation hosting cultural heritage sites from Central India using remote sensing. *Land Use Policy* **2013**, *34*, 193–203. [[CrossRef](#)]
25. Bai, X.; Du, P.; Guo, S.; Zhang, P.; Lin, C.; Tang, P.; Zhang, C. Monitoring land cover change and disturbance of the Mount Wutai world cultural landscape heritage protected area, based on remote sensing time-series images from 1987 to 2018. *Remote Sens.* **2019**, *11*, 1332. [[CrossRef](#)]
26. Assassi, A.; Mebarki, A. Spatial configuration analysis via digital tools of the archeological roman town timgad, algeria. *Mediterr. Archaeol. Archaeom.* **2021**, *21*, 71–84.
27. Diwan, G.A. GIS-based comparative archaeological predictive models: A first application to iron age sites in the bekaa (Lebanon). *Mediterr. Archaeol. Archaeom.* **2020**, *20*, 143–158.
28. Hadjimitsis, D.; Agapiou, A.; Alexakis, D.; Sarris, A. Exploring natural and anthropogenic risk for cultural heritage in Cyprus using remote sensing and GIS. *Int. J. Digit. Earth* **2013**, *6*, 115–142. [[CrossRef](#)]
29. Agapiou, A.; Lysandrou, V.; Alexakis, D.D.; Themistocleous, K.; Cuca, B.; Argyriou, A.; Sarris, A.; Hadjimitsis, D.G. Cultural heritage management and monitoring using remote sensing data and GIS: The case study of Paphos area, Cyprus. *Comput. Environ. Urban Syst.* **2015**, *54*, 230–239. [[CrossRef](#)]
30. Elfadaly, A.; Eldein, A.S.; Lasaponara, R. Cultural heritage management using remote sensing data and GIS techniques around the archaeological area of Ancient Jeddah in Jeddah City, Saudi Arabia. *Sustainability* **2019**, *12*, 240. [[CrossRef](#)]
31. Moise, C.; Negula, I.D.; Mihalache, C.E.; Lazar, A.M.; Dedulescu, A.L.; Rustoiu, G.T.; Inel, I.C.; Badea, A. Remote Sensing for Cultural Heritage Assessment and Monitoring: The Case Study of Alba Iulia. *Sustainability* **2021**, *13*, 1406. [[CrossRef](#)]
32. Chen, W.; Huang, H.P.; Tian, Y.C.; Du, Y.Y. Monitoring and assessment of the eco-environment quality in the Sanjiangyuan region based on Google Earth Engine. *J. Geo Inf. Sci.* **2019**, *21*, 1382–1391.
33. Aminzadeh, B.; Samani, F. Identifying the boundaries of the historical site of Persepolis using remote sensing. *Remote Sens. Environ.* **2006**, *102*, 52–62. [[CrossRef](#)]
34. Themistocleous, K. Multi-temporal study of archaeological sites in Cyprus using atmospheric corrected satellite remotely sensed data. *Int. J. Archit. Comput.* **2009**, *7*, 121–138.
35. Figorito, B.; Tarantino, E. Semi-automatic detection of linear archaeological traces from orthorectified aerial images. *Int. J. Appl. Earth Obs. Geoinf.* **2014**, *26*, 458–463. [[CrossRef](#)]
36. Luo, L.; Wang, X.; Liu, C.; Guo, H.; Du, X. Integrated RS, GIS and GPS approaches to archaeological prospecting in the Hexi Corridor, NW China: A case study of the royal road to ancient Dunhuang. *J. Archaeol. Sci.* **2014**, *50*, 178–190. [[CrossRef](#)]
37. Crutchley, S.; Crow, P. *The Light Fantastic: Using Airborne Lidar in Archaeological Survey*; English Heritage: Swindon, UK, 2010.
38. Takeshi, I.; Flory, P.; Luis, R.J.; Tsuyoshi, H.; Hiroo, N.; Carlos, F.D.J.; Kazuo, A.; Hitoshi, Y. Archaeological application of airborne LiDAR with object-based vegetation classification and visualization techniques at the lowland Maya site of Ceibal, Guatemala. *Remote Sens.* **2017**, *9*, 563.
39. Canuto, M.A.; Estrada-Belli, F.; Garrison, T.G.; Houston, S.D.; Acuña, M.J.; Kováč, M.; Marken, D.; Nondédéo, P.; Auld-Thomas, L.; Castanet, C.; et al. Ancient lowland Maya complexity as revealed by airborne laser scanning of northern Guatemala. *Science* **2018**, *361*, 1355. [[CrossRef](#)] [[PubMed](#)]
40. Vinci, G.; Bernardini, F. Reconstructing the protohistoric landscape of Trieste Karst (north-eastern Italy) through airborne LiDAR remote sensing. *J. Archaeol. Sci. Rep.* **2017**, *12*, 591–600.
41. Trier, I.D.; Reksten, J.H.; Lseth, K. Automated mapping of cultural heritage in Norway from airborne LiDAR data using faster R-CNN. *Int. J. Appl. Earth Obs. Geoinf.* **2021**, *95*, 102241. [[CrossRef](#)]
42. Tsiafaki, D.; Michailidou, N. Benefits and problems through the application of 3d technologies in archaeology: Recording, visualisation, representation and reconstruction. *Sci. Cult.* **2015**, *1*, 37–45.

43. Hatzopoulos, J.N.; Stefanakis, D.; Georgopoulos, A.; Tapinaki, S.; Pantelis, V.; Liritzis, I. Use of various surveying technologies to 3d digital mapping and modelling of cultural heritage structures for maintenance and restoration purposes: The tholos in DELPHI, GREECE. *Mediterr. Archaeol. Archaeom.* **2017**, *17*, 311–336.
44. Altuntas, C.; Hezer, S.; Kırılı, S. Image based methods for surveying heritage of masonry arch bridge with the example of dokuzunhan in konya, Turkey. *Sci. Cult.* **2017**, *3*, 13–20.
45. Vilbig, J.M.; Sagan, V.; Bodine, C. Archaeological surveying with airborne LiDAR and UAV photogrammetry: A comparative analysis at Cahokia Mounds. *J. Archaeol. Sci. Rep.* **2020**, *33*, 102509. [[CrossRef](#)]
46. Su, T.C. Environmental risk mapping of physical cultural heritage using an unmanned aerial remote sensing system: A case study of the Huang-Wei monument in Kinmen, Taiwan. *J. Cult. Herit.* **2019**, *39*, 140–151. [[CrossRef](#)]
47. Zhen, J.; Wang, X.; Meng, Q.; Song, J.; Ying, L.; Bo, X.; Guo, H.; Liu, C.; Yang, R.; Lei, L. Fine-Scale Evaluation of Giant Panda Habitats and Countermeasures against the Future Impacts of Climate Change and Human Disturbance (2015–2050): A Case Study in Ya'an, China. *Sustainability* **2018**, *10*, 1081. [[CrossRef](#)]
48. Roy, N.; Pandey, B.W.; Rani, U. Protecting the vanishing geo-cultural heritage of India: Case study of Majuli Island in Assam. *Int. J. Geoheritage Parks* **2020**, *8*, 18–30. [[CrossRef](#)]
49. Iriarte, E.; Sánchez, M.Á.; Foyo, A.; Tomillo, C. Geological risk assessment for cultural heritage conservation in karstic caves. *J. Cult. Herit.* **2010**, *11*, 250–258. [[CrossRef](#)]
50. Rodríguez-Rosales, B.; Abreu, D.; Ortiz, R.; Becerra, J.; Cepero-Acán, A.E.; Vázquez, M.A.; Ortiz, P. Risk and vulnerability assessment in coastal environments applied to heritage buildings in Havana (Cuba) and Cadiz (Spain). *Sci. Total Environ.* **2021**, *750*, 141617. [[CrossRef](#)]
51. Nebbia, M.; Cilio, F.; Bobomulloev, B. Spatial risk assessment and the protection of cultural heritage in southern Tajikistan. *J. Cult. Herit.* **2021**. [[CrossRef](#)]
52. Friedl, M.A.; Brodley, C.E. Decision tree classification of land cover from remotely sensed data. *Remote Sens. Environ.* **1997**, *61*, 399–409. [[CrossRef](#)]
53. Deardorff, J.W. Efficient prediction of ground surface temperature and moisture, with inclusion of a layer of vegetation. *J. Geophys. Res.* **1978**, *83*, 1889–1904. [[CrossRef](#)]
54. Gutman, G.; Ignatov, A. The derivation of the green vegetation fraction from NOAA/AVHRR data for use in numerical weather prediction models. *Int. J. Remote Sens.* **1998**, *19*, 1533–1543. [[CrossRef](#)]
55. Zhang, M.; Wang, J.; Li, S. Tempo-spatial changes and main anthropogenic influence factors of vegetation fractional coverage in a large-scale opencast coal mine area from 1992 to 2015. *J. Clean. Prod.* **2019**, *232*, 940–952. [[CrossRef](#)]
56. Song, Y.; Lu, Y.; Liu, T.; Li, H.; Yue, Z.; Liu, H.; Gao, T. Variation of vegetation fractional coverage and its relationship with climate in a desert steppe: Optimization of farmland layout in a farming–pastoral ecotone using the ecological suitability index. *Ecol. Eng.* **2020**, *150*, 105834. [[CrossRef](#)]
57. Ministry of Water Resources, PRC. *Soil Erosion Classification and Grading Standards, SL190-2007*; China Water Power Press: Beijing, China, 2008.
58. Hu, Z.; He, F.; Yin, J.; Lu, X.; Tang, S.; Wang, L.; Li, X. Estimation of fractional vegetation cover based on digital camera survey data and a remote sensing model. *J. China Univ. Min. Technol.* **2007**, *1*, 116–120. [[CrossRef](#)]
59. Wang, F.; Yeap, S.P. Using magneto-adsorbent for methylene Blue removal: A decision-making via analytical hierarchy process (AHP). *J. Water Process Eng.* **2021**, *40*, 101948. [[CrossRef](#)]
60. Saaty, R.W. The analytic hierarchy process—What it is and how it is used. The analytic hierarchy process. *Math. Model.* **1987**, *9*, 161–176. [[CrossRef](#)]